



Bidirectional photocurrent in p–n heterojunction nanowires

Danhao Wang¹, Xin Liu¹, Yang Kang¹, Xiaoning Wang², Yuanpeng Wu³, Shi Fang¹, Huabin Yu¹, Muhammad Hunain Memon¹, Haochen Zhang¹, Wei Hu², Zetian Mi³, Lan Fu⁴, Haiding Sun¹✉ and Shibing Long¹

Semiconductor p–n junctions provide rectification behaviour and act as building blocks in many electronic devices. However, the typical junction configuration restricts the potential functionalities of devices. Here we report a light-detection electrochemical cell that is based on vertically aligned p-AlGaIn/n-GaN p–n heterojunction nanowires in an electrolyte environment. After decorating the nanowires with platinum nanoparticles, the cell exhibits a photoresponse in which the photocurrent polarity is reversed depending on the wavelength of light. In particular, illumination of the device at two different wavelengths (254 nm and 365 nm) triggers different redox reactions at the nanowire/electrolyte interface, inducing polarity reversal of the photocurrent. The device offers a responsivity of up to -175 mA W^{-1} at 254 nm and 31 mA W^{-1} at 365 nm, both at 0 V.

The semiconductor p–n junction is a fundamental building block in numerous electronic components, including rectifiers/diodes, photovoltaic cells, light-emitting diodes (LEDs) and photodetectors^{1–3}. All p–n junction-based devices must, however, obey the physics of unidirectional current flow, which constrains the possible functionalities of devices. As a result, various modified device designs have been developed over the last few decades. The bipolar junction transistor (a semiconductor triode), which can amplify or switch electronic signals, was—for a start—created⁴, and it laid the foundation for integrated circuits. The efficiency of a single p–n junction photovoltaic cell is, similarly, intrinsically limited. However, by designing multi-junction devices with series-connected/tandem cells, remarkable power conversion efficiencies—beyond the fundamental limitation of single-junction solar cells—have been achieved in a range of material systems (including silicon, III–Vs and perovskite solar cells)^{5–8}. Recently, such multi-junction or tandem strategies have also been applied in dual light-emitting and detecting optoelectronic devices within a single structure for energy-harvesting displays⁹.

When combined with the photoelectric effect, p–n junctions can be used to build solid-state photodetectors. However, the detection capabilities of such devices are constrained to a certain spectrum range due to two basic working principles: the incident photon energy needs to be larger than the bandgap of the semiconductor, and the resultant photocurrent flows in the same direction (unipolar photoresponse) under a certain applied bias voltage^{1,10–12}. To break the limit of conventional p–n junction-based photodetectors, wavelength-induced photocurrent polarity switching in solid-state p–n heterojunctions made of SnS/ZnO (ref. ¹³) and Sb₂Se₃/ZnO (ref. ¹⁴) semiconductors has been developed; the capabilities of such devices can be attributed to the competition between photovoltaic and photothermoelectric effects in the junction¹⁵. These results suggest that bidirectional photocurrent behaviour could be used in

applications such as switchable light imaging and optical communication, as well as filter-less colour discrimination.

In this Article, we report a light-detection electrochemical cell based on uniform and vertically aligned p-AlGaIn/n-GaN p–n heterojunction nanowires. After decorating the nanowires with platinum (Pt) nanoparticles, the junctions are exposed to an electrolyte environment that acts like a third electrode (analogous to the third electrode in a bipolar junction transistor), and a distinctive photoresponse with reversed polarity from the cell under different light exposures can be observed at a constant applied bias. Illumination of the device at two different wavelengths (254 and 365 nm) triggers opposite redox reactions at the nanowire/electrolyte interface, inducing polarity reversal of the photocurrent. The device exhibits a responsivity of up to -175 mA W^{-1} at 254 nm and 31 mA W^{-1} at 365 nm, both at 0 V. The resulting photodetector operates under a combination of physical processes (photoelectric conversion and carrier transport in a single p–n junction) and chemical process (redox reaction on the nanowire surface), and provides a fast approach to distinguish different spectral bands by simply verifying the polarity of the photocurrent.

Construction of light-detection electrochemical cell

Our light-detection electrochemical cell is composed of p-AlGaIn/n-GaN nanowires grown on n-type Si(111) (Supplementary Fig. 1). Each nanowire consists of a 200 nm Si-doped n-GaN and a 200 nm Mg-doped p-AlGaIn segment along the axial direction (Fig. 1b and Supplementary Fig. 1). The top p-AlGaIn segment with an aluminium composition of ~35% is specifically designed to absorb light within the deep ultraviolet band (for example, 254 nm light used for our test), which can also be absorbed by the underlying n-GaN segment. Lower-energy photons (such as the 365 nm light used for our test) can only be absorbed by the bottom n-GaN part since the p-AlGaIn segment

¹School of Microelectronics, University of Science and Technology of China, Hefei, People's Republic of China. ²Hefei National Laboratory for Physical Sciences at the Microscale, Department of Chemical Physics, University of Science and Technology of China, Hefei, People's Republic of China.

³Department of Electrical Engineering and Computer Science, University of Michigan, Ann Arbor, MI, USA. ⁴Department of Electronic Materials Engineering, Research School of Physics and Engineering, The Australian National University, Canberra, Australian Capital Territory, Australia.

✉e-mail: haiding@ustc.edu.cn

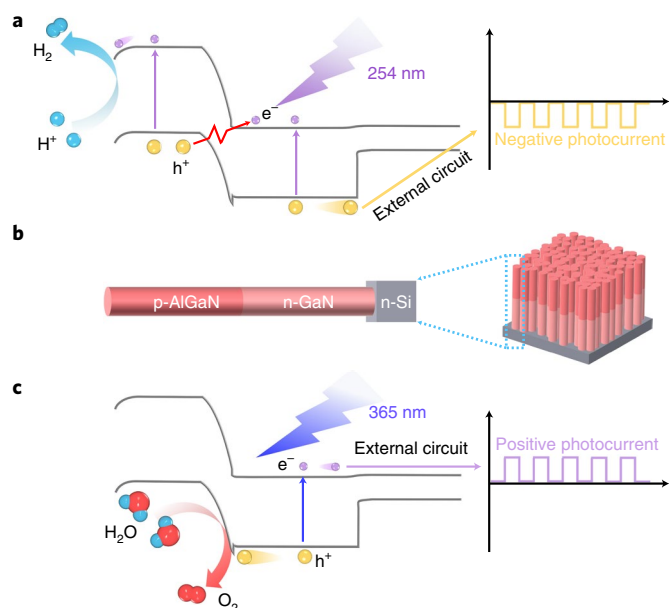


Fig. 1 | Design of p-AlGaIn/n-GaN nanowires for light-detection electrochemical cell. **a**, Operation model of the cell under 254 nm irradiation. The energy band diagrams, light-induced photocarrier excitation, carrier recombination through tunnelling, carrier diffusion process, proton reduction at the p-AlGaIn surface and corresponding negative photocurrent signal are shown. **b**, Schematic of the as-grown p-AlGaIn/n-GaN nanowires on n-Si substrate. **c**, Operation model of the cell under 365 nm irradiation along with the energy band diagrams, light-induced photocarrier excitation, carrier diffusion process, water oxidation at the n-GaN surface and corresponding positive photocurrent signal.

is transparent to the 365 nm light. Additionally, the n-Si substrate also plays an important role for efficient carrier transport because of the relatively small band offset between the n-Si and n-GaN conduction band edges^{16,17}. Then, the as-grown p-AlGaIn/n-GaN nanowires act as photoelectrodes to construct the light-detection electrochemical cell.

The cell operates differently from conventional p-n junction-based photodetectors, mainly due to its electrolyte-assisted carrier transport characteristic arising from a combination of physical and chemical processes. Figure 1a,c describes the detailed working principle of the light-detection electrochemical cell operating under exposure of different wavelengths of light. The energy band diagrams along the growth direction and the corresponding photocurrent signals are also schematically illustrated. When p-AlGaIn/n-GaN nanowires are illuminated with 254 nm light, electron-hole pairs are generated in both p-AlGaIn and n-GaN segments (Fig. 1a). The downward surface band bending facilitates electrons in the p-AlGaIn segment drifting towards the nanowire surface to drive the proton reduction reaction (hydrogen evolution reaction (HER))¹⁸, while the holes migrate towards the space charge region in the p-n junction, efficiently tunnelling and recombining with electrons generated from the n-GaN segment. Simultaneously, the photogenerated holes in the n-GaN segment migrate through the external circuit and oxidize the water molecules into oxygen at the Pt counter electrode, hence exhibiting a negative photocurrent signal (Supplementary Fig. 2a).

When the nanowires are exposed to 365 nm light, the operation mechanism is entirely different (Fig. 1c). Since only the n-GaN segment can absorb 365 nm light, the photogenerated holes in n-GaN readily drift to the n-GaN/electrolyte interface and undergo water oxidation reaction (oxygen evolution reaction (OER)), with the

upward surface band bending as the driving force¹⁸. Meanwhile, band bending at the n-GaN/electrolyte interface and built-in electric field of the p-n junction push electrons drifting towards the external circuit, recorded as a positive photocurrent through the electrochemical workstation. These electrons eventually participate in HER at the counter electrode (Supplementary Fig. 2b).

Essentially, the axial p-n heterojunction nanowire configuration is critical for constructing a light-detection electrochemical cell. We can benefit from the flexibility in tailoring the bandgap of each segment in the nanowires by choosing proper semiconductor materials, as well as the direct contact of all the nanowire segments with the electrolyte environment for electrochemical reactions. Such a design makes it possible to distinguish spectral regimes by monitoring the polarity of the photocurrent arising from different redox reactions. In this work, the p-AlGaIn/n-GaN p-n heterojunction nanowires were grown on silicon by a plasma-assisted molecular beam epitaxy (MBE) system (Supplementary Note and Supplementary Fig. 3 provide a detailed discussion of the growth process and crystalline quality of nanowires).

Theoretical calculations

Unlike conventional p-n junction photodetectors, which rely only on the photoelectric effect for light detection, the photocurrent of a nanowire-based light-detection electrochemical cell is determined by the number of photogenerated carriers that participate in the redox reactions. In other words, the magnitude of the photocurrent is affected by the number of photogenerated carriers as well as the redox reaction rates. Generally, the rate of HER is mainly determined by the hydrogen adsorption free energy, ΔG_{H} (ref. 19). Unfortunately, the adsorption energies of the reactive intermediates on bare p-AlGaIn nanowire surface are not suitable for HER. To boost the detection efficiency of 254 nm light, a modification of the ΔG_{H} value of the p-AlGaIn segment is required.

In the past few decades, it has been recognized that co-catalysts play an essential role in boosting the electrochemical reaction rates. Through co-catalyst decoration, the adsorption energies of reactive intermediates and carrier separation efficiency can be simultaneously improved²⁰. Thus, we conducted theoretical investigations based on density functional theory (DFT) calculations and found that Pt nanoparticles could be one of the most efficient proton reduction co-catalysts to decorate the AlGaIn surface. Figure 2a shows the calculated Gibbs free energy of the adsorption of intermediate hydrogen of AlGaIn(000 $\bar{1}$)/Pt and AlGaIn(000 $\bar{1}$). Figure 2b,c depicts the corresponding atomic configurations of one H⁺ adsorption step. Obviously, the AlGaIn(000 $\bar{1}$)/Pt model exhibits a relatively low barrier for the Volmer step, with an energy barrier of -0.38 eV. In contrast, the energy barrier is as high as -2.177 eV on a bare AlGaIn(000 $\bar{1}$) surface. This result indicates that by incorporating Pt nanoparticles on the AlGaIn(000 $\bar{1}$) surface, the proton reduction thermodynamics can be optimized to facilitate the HER process.

To achieve high photodetection performance, charge separation efficiency should also be considered. Fortunately, in addition to the reduced proton reduction barrier, Pt nanoparticles can also improve the charge separation and extraction efficiency²¹. Differential charge density analysis was carried out to elucidate the interaction between Pt nanoparticles and AlGaIn alloy. Figure 2d illustrates that the accumulation of charge (red region) occurs at the Pt atoms/AlGaIn interface while charge reduction (blue region) is found around the Pt and N atoms, revealing that the electrons are apparently shared by both Pt and AlGaIn alloy, which results in new hybridized states in the forbidden band²². To further confirm the newly induced electronic states, the density of states for AlGaIn bulk, AlGaIn(000 $\bar{1}$) surface and AlGaIn(000 $\bar{1}$)/Pt was calculated based on the DFT method. First, the near-perfect agreement of the calculated bandgap (4.252 eV; Supplementary Fig. 4) of AlGaIn bulk with its experimental value (4.2 eV; Supplementary Fig. 3) verifies

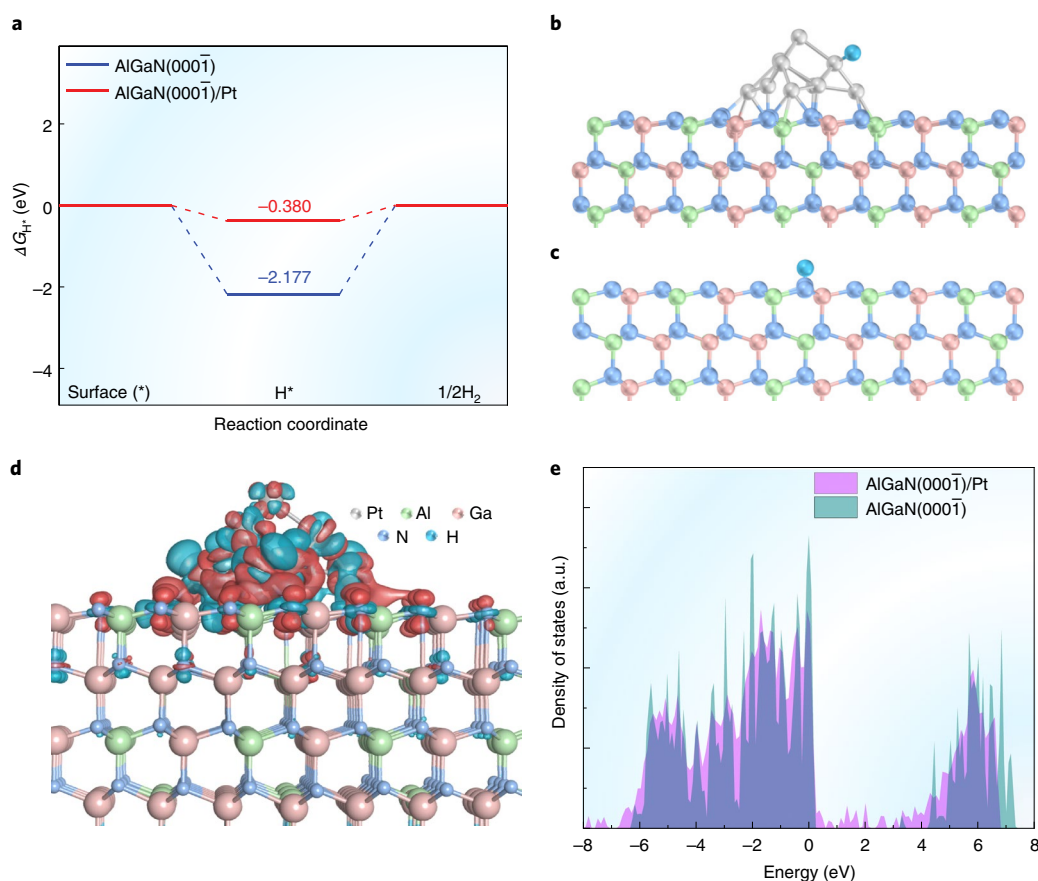


Fig. 2 | DFT calculations. **a**, Calculated adsorption energies of intermediate hydrogen on the AlGaN(000 $\bar{1}$)/Pt and AlGaN(000 $\bar{1}$) surface. **b,c**, Corresponding atomic configurations of the proton adsorption step on the AlGaN(000 $\bar{1}$)/Pt (**b**) and AlGaN(000 $\bar{1}$) (**c**) surface. The spheres in sky blue, green, pink, royal blue and white represent H, Al, Ga, N, and Pt atoms, respectively. **d**, Charge density difference plot of AlGaN(000 $\bar{1}$)/Pt. The blue and red regions represent the deletion and accumulation of electrons, respectively. **e**, Calculated density of states of AlGaN(000 $\bar{1}$) (blue area) and AlGaN(000 $\bar{1}$)/Pt (pink area).

the high accuracy of our simulation methods and models. Secondly, the density of states for AlGaN(000 $\bar{1}$) (blue area) presents a classic semiconductor characteristic with a bandgap of approximately 4 eV, as shown in Fig. 2e. A detailed explanation about the small peak in the forbidden band can be found in Supplementary Fig. 5.

Lastly, when the Pt nanoparticle is anchored on the AlGaN(000 $\bar{1}$) surface, new states in the bandgap can be observed (pink area), indicating the formation of new migration channels for carrier transfer from AlGaN to the Pt nanoparticle, eventually reaching the electrolyte²¹. All these results suggest that the decoration of Pt nanoparticles endows the device with ideal hydrogen adsorption free energy as well as highly efficient charge carrier extraction during the photoelectrochemical light detection process.

Pt decoration and structural characterization

Based on the theoretical guidance, we modified the as-grown bare p-AlGaN/n-GaN nanowire surface through Pt nanoparticle decoration using selective photochemical deposition, during which Pt nanoparticles anchored on the surface sites where electrons had selectively accumulated^{23–26}. Figure 3a shows a schematic of the photochemical deposition process. In principle, when the nanowires are in contact with the electrolyte, downward and upward surface band bending happen in the p-AlGaN and n-GaN segments, respectively. Therefore, only the p-AlGaN surface accumulates electrons that are photogenerated by the incident ultraviolet light^{18,27}. In other words, Pt nanoparticles are preferentially photodeposited on the p-AlGaN

surface due to the intrinsic selectivity of photochemical deposition. Compared with other random synthesis methods (for example, chemical reduction), the photodeposition approach is more favourable for photogenerated electrons to drift to the photochemically deposited active sites and participate in the HER process^{25,26}.

To elucidate the chemical nature of the as-decorated Pt species, the valence states of Pt were investigated by X-ray photoelectron spectroscopy (XPS). As shown in Fig. 3b, the Pt4f XPS spectrum of Pt-decorated p-AlGaN/n-GaN nanowires could be assigned as a mixture of Pt⁰ and Pt²⁺ species, corresponding to metallic Pt and Pt(II)O species, respectively²⁶. The decrease in the valence state with respect to the Pt precursor (H₂PtCl₆), as shown in Fig. 3b, indicates that PtCl₆²⁻ ions were effectively photoreduced by the photo-generated electrons. Scanning electron microscopy (SEM) images clearly indicate that the Pt nanoparticles were selectively formed on the p-AlGaN segment (as shown in Fig. 3c), tending to deposit on the top surface of the AlGaN(000 $\bar{1}$) segment. To further characterize the structural properties of our Pt:p-AlGaN/n-GaN nanowires, we carried out scanning transmission electron microscopy (STEM) measurements. It can be seen that the Pt nanoparticles are preferentially distributed on the top surface of the p-AlGaN(000 $\bar{1}$) segment (Fig. 3d).

Previous studies reported that when the co-catalysts are selectively deposited on the corresponding electron-concentrated segment, the redox reaction could be enhanced because electrons tend to be trapped on the co-catalysts, inducing more efficient

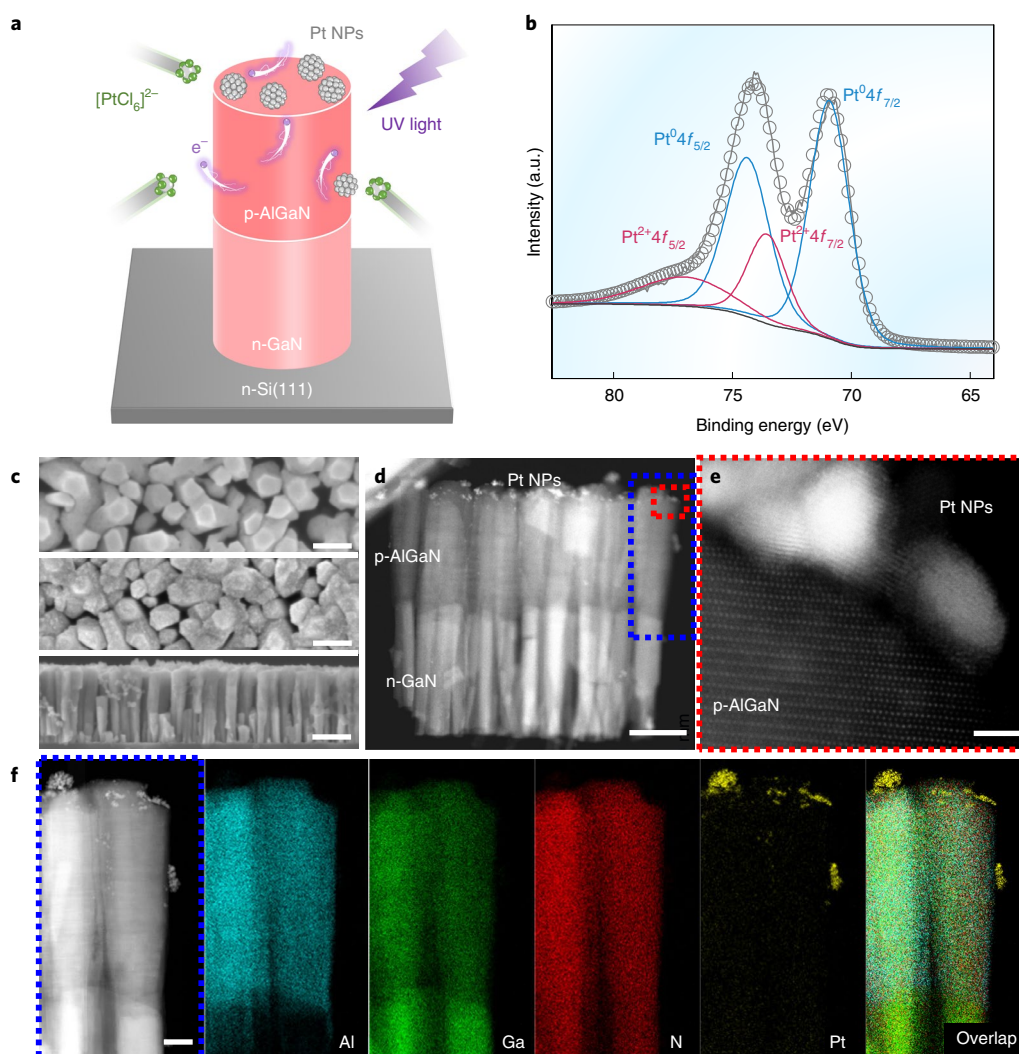


Fig. 3 | Photodeposition process and structural characterization of nanowires. **a**, Schematic of the photodeposition method to form Pt nanoparticles (Pt NPs) on a p-AlGaIn/n-GaN nanowire. **b**, XPS spectra of Pt:p-AlGaIn/n-GaN nanowires. High-resolution Pt4f spectra is fitted by the spin-orbit splitting of 3.45 eV and the area ratio of 4:3 for Pt4f_{7/2} and Pt4f_{5/2}. **c**, Top-view SEM images of bare p-AlGaIn/n-GaN nanowires (top; scale bar, 100 nm), Pt-decorated p-AlGaIn/n-GaN nanowires (middle; scale bar, 100 nm) and side-view cross-sectional image of Pt:p-AlGaIn/n-GaN nanowires (bottom; scale bar, 200 nm). **d,e**, Overview of the STEM image of Pt-decorated nanowires (**d**; scale bar, 100 nm) and atomic-resolution HAADF-STEM image of the top part of Pt:p-AlGaIn/n-GaN nanowires (**e**; scale bar, 2 nm). **f**, Selected-area STEM image and the corresponding EDS elemental mapping images (scale bar, 30 nm).

charge separation^{20,25}. On the contrary, the photocurrent would be drastically decreased if co-catalysts were deposited on the wrong segment²⁶. Therefore, in our case, a boosted photodetection performance could be expected, as the Pt nanoparticles are mainly located at the p-AlGaIn surface. Detailed high-resolution high-angle annular dark-field scanning transmission electron microscopy (HAADF-STEM) images indicate that the crystalline Pt nanoparticles have a particle size of ~4 nm (Fig. 3e), with two distinct interplanar spacings, namely, 2.3 and 2 Å (Supplementary Fig. 6), which could be assigned to Pt(111) and Pt(100), respectively^{28,29}. More importantly, the energy-dispersive spectroscopy (EDS) elemental mapping analysis of the STEM images directly confirms the preferential distribution of Pt nanoparticles on p-AlGaIn/n-GaN nanowires (Fig. 3f).

To provide an insight into the carrier transport properties of p-AlGaIn/n-GaN nanowires before and after Pt decoration, we carried out electrochemical impedance spectroscopy measurements under 254 nm illumination. It is known that the diameter of the semicircle in a Nyquist plot is a characteristic of the charge

transfer resistance³⁰. As shown in Supplementary Fig. 7, the radius of Pt:p-AlGaIn/n-GaN nanowires is much smaller than that of p-AlGaIn/n-GaN nanowires, thus providing unambiguous evidence that Pt decoration can reduce the resistivity of electron transfer²². Meanwhile, Pt nanoparticles can serve as an effective charge storage medium for facile charge transfer from the p-AlGaIn segment to the electrolyte²¹. Furthermore, we investigated the carrier characteristics of as-grown and Pt-decorated nanowires by room-temperature photoluminescence (PL) spectroscopy. It is widely recognized that the PL peak intensity effectively reflects the carrier trapping, migration, transfer and recombination efficiency, and it is directly correlated with the photorelated electrochemical performance^{31,32}. Supplementary Fig. 8 clearly shows the reduction in the PL peak intensity after Pt loading, which confirms the effective carrier separation or a suppression of the carrier recombination^{18,33}.

Behaviour of spectrally distinctive photodetection

Based on our band structure design, theoretical calculations and material characterization, the p-AlGaIn/n-GaN nanowire-based

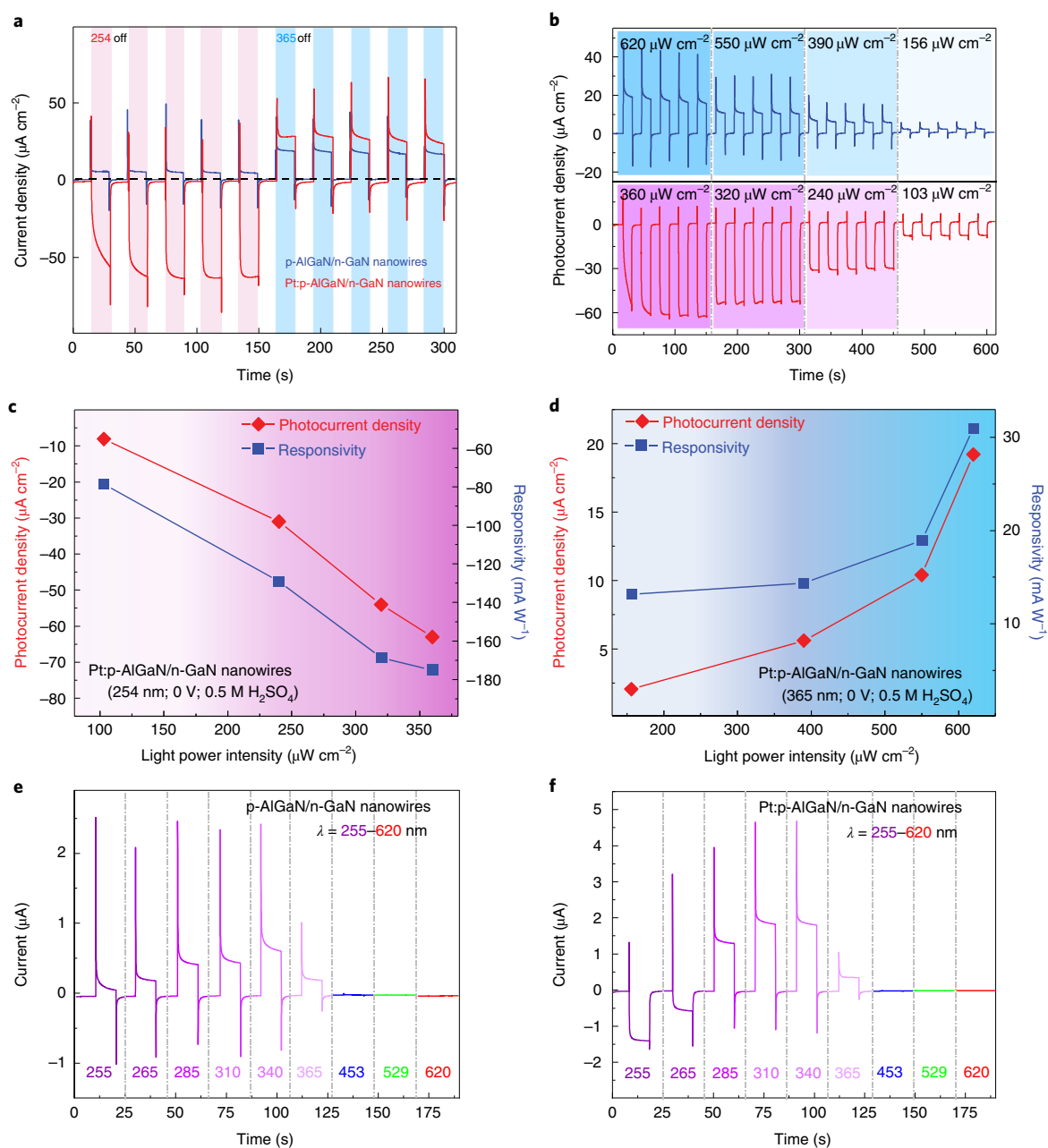


Fig. 4 | Spectrally distinctive photodetection characterization. **a**, Repeated on-off I - t characteristics of p-AlGaIn/n-GaN nanowires-based and Pt:p-AlGaIn/n-GaN nanowires-based light-detection electrochemical cell at 0 V under 254 nm and 365 nm light illumination. **b**, I - t characteristics of Pt:p-AlGaIn/n-GaN nanowires-based light-detection electrochemical cell at 0 V under 254 nm and 365 nm light illumination with different light intensities. **c,d**, Extracted photocurrent density and corresponding photoresponsivity of Pt:p-AlGaIn/n-GaN nanowires under 254 nm (**c**) and 365 nm (**d**) irradiation with different light intensity. **e,f**, Current signals of p-AlGaIn/n-GaN nanowires (**e**) and Pt:p-AlGaIn/n-GaN nanowires (**f**) under LED illuminations at different wavelengths (λ).

photoelectrodes were employed to construct the light-detection electrochemical cell (Supplementary Fig. 9) and applied for the detection test of 254/365 nm light. To present a thorough and comprehensive understanding of the wavelength-dependent polarity switching of the photocurrent, we performed the current-time response (I - t curves) test of our light-detection electrochemical cell with multiple light-switching cycles under 0 V. With periodically switched light, the I - t curves of both p-AlGaIn/n-GaN and Pt:p-AlGaIn/n-GaN nanowires demonstrated repeatable on-off switching behaviour.

Figure 4a shows the photoresponse of p-AlGaIn/n-GaN nanowires and Pt:p-AlGaIn/n-GaN nanowires under 254 and 365 nm illumination at 0 V. Bare p-AlGaIn/n-GaN nanowires exhibit a positive current density of $18.7 \mu\text{A cm}^{-2}$ under 365 nm illumination, while the current in the solar-blind region becomes much smaller with a current density of only $5.6 \mu\text{A cm}^{-2}$. Importantly, both photoresponses are unipolar, showing a unidirectional current transient response. When it comes to the Pt:p-AlGaIn/n-GaN nanowires, the photocurrent polarity can be reversed once the incident light changes from 365 to 254 nm. The Pt:p-AlGaIn/n-GaN nanowires

show a positive current density of $23 \mu\text{A cm}^{-2}$ under 365 nm illumination, whereas a negative current density of $-64 \mu\text{A cm}^{-2}$ under 254 nm illumination.

Notably, there are photocurrent peaks in both $I-t$ response curves. Such transient photocurrent peaks in the photoelectrochemical cell might be attributed to the transient carrier accumulation and recombination near the semiconductor/electrolyte interface through the trapping of electrons/holes at the surface states^{34,35}. Alternatively, it might be caused by the pyroelectric effect because such transient photocurrent peaks were also observed in ZnO-based pyroelectric photodetectors³⁶. Since our GaN-based nanowires also possess strong pyroelectricity effect and additionally, the size and shape of the nanowires can also influence the pyroelectric properties in nitride nanowires³⁷, we suspect that the pyroelectric effect of p-AlGaIn/n-GaN nanowires, therefore, may lead to such transient photocurrent peaks. Nevertheless, the dual-polarity photoresponse behaviour in our electrochemical cell can be implemented in light-induced photocurrent polarity-switchable devices for light imaging system, visible-light communication and accurate indoor positioning applications^{13,14}. Moreover, such a cell can be further miniaturized by choosing nanowire arrays with high periodicity and uniformity in device fabrication³⁸, which could lead to next-generation high-pixel, high-resolution imaging/sensors.

To further characterize the photodetection performance, we define photocurrent density I_{photo} as follows³⁹: $I_{\text{photo}} = I_{\text{light}} - I_{\text{dark}}$, where I_{light} and I_{dark} are the current density with or without light, respectively, as extracted from the $I-t$ curves. The light-intensity-dependent photocurrent $I_{\text{photo-254}}$ under different 254 nm light intensity ($P_{\text{opt-254}}$) varying from 103 to $360 \mu\text{W cm}^{-2}$ and $I_{\text{photo-365}}$ under different 365 nm light intensity ($P_{\text{opt-365}}$) varying from 156 to $620 \mu\text{W cm}^{-2}$ were then evaluated. The relationship between $I_{\text{photo-254}}$, $I_{\text{photo-365}}$ and irradiance power intensity is presented in Fig. 4b. It can be found that both $I_{\text{photo-254}}$ and $I_{\text{photo-365}}$ exhibit a positive correlation trend with continuously increasing light power density, showing potential for light intensity quantification. The $I_{\text{photo-254}}$ value can reach up to $-63.4 \mu\text{A cm}^{-2}$ at $P_{\text{opt-254}} = 360 \mu\text{W cm}^{-2}$ and the $I_{\text{photo-365}}$ value is $19.2 \mu\text{A cm}^{-2}$ at $P_{\text{opt-365}} = 620 \mu\text{W cm}^{-2}$. Figure 4c,d shows the I_{photo} and responsivity (R) values as a function of different P_{opt} values. The responsivity was calculated as follows³⁹: $R = I_{\text{photo}}/P_{\text{opt}}$, where I_{photo} is the photocurrent density and P_{opt} is the corresponding incident light intensity. Along with ramping up of the incident irradiation, the responsivity of Pt:p-AlGaIn/n-GaN nanowires under 254 nm illumination increases from -79 to -175 mA W^{-1} , while the responsivity increases from 13 to 31 mA W^{-1} under 365 nm illumination. We also performed the durability test of our device and the results are discussed in Supplementary Fig. 10a,b.

To confirm the switching point of photocurrent polarity, we measured and compared the output current under different light illuminations. Figures 4e,f presents the measured current signals of p-AlGaIn/n-GaN nanowires and Pt:p-AlGaIn/n-GaN nanowires under LED illuminations with different wavelengths at 0 V in 0.5 M H_2SO_4 . It shows that the photocurrent of bare p-AlGaIn/n-GaN nanowires exhibits a constant positive polarity (Fig. 4e), while the photocurrent polarity of Pt-decorated p-AlGaIn/n-GaN nanowires is highly dependent on the wavelength of incident light (Fig. 4f). First, we observed negative current signals on light illuminations with wavelengths lower than 265 nm. Thereafter, when the device was exposed to light with longer wavelengths (285 nm or higher), the photocurrent polarity was reversed from negative to positive, which exactly follows the working principle illustrated in Fig. 1. This phenomenon confirms the success of our device design for distinguishing spectral bands by simply measuring the polarity of the photocurrent. Besides, the photocurrent corresponding to visible-light irradiation (incident light wavelength is 453 nm or higher) can be negligible, which reflects the excellent visible-blind characteristic of our device.

Moreover, in a classic solid-state photodetector, photoresponse can be merely tuned by changing the applied voltage or incident light intensity. For our light-detection electrochemical cells, essentially, their photocurrent can also be easily tuned by the surrounding environment, especially the electrolyte, which has a profound effect on the photoresponse behaviour. In Supplementary Fig. 10c,d, the value of $I_{\text{photo-254}}$ has a linear relationship with increasing H_2SO_4 concentration, while $I_{\text{photo-365}}$ is maintained at a constant level, which demonstrates that our light-detection electrochemical cell is also sensitive to the electrolyte concentration. Such additional tunability could further broaden the application of our devices towards complex optical and imaging sensing applications in a sophisticated environment. In short, all the above features demonstrate that Pt:p-AlGaIn/n-GaN nanowires exhibit great potential for spectrally selective and sensitive applications.

Conclusions

We have reported bidirectional photoconductivity behaviour in a light-detection electrochemical cell composed of Pt-decorated p-AlGaIn/n-GaN nanowires. The reversal of the flow of photocurrent is triggered by diverse redox reactions at the nanowire/electrolyte interface under different light illuminations: under 254 nm illumination, the nanowires exhibit a negative responsivity of -175 mA W^{-1} , whereas under 365 nm illumination, the nanowires exhibit a positive responsivity of 31 mA W^{-1} , both at 0 V. This bipolar photoconductivity behaviour illustrates that vertical p-n junction nanowires can provide spectral-band-distinguishable photodetection. Our device architecture could potentially provide distinct responses to ultraviolet, visible and infrared illumination by constructing nanowire p-n heterojunctions based on a combination of binary or ternary III-V semiconductors with different material compositions (such as III-nitrides or III-arsenides). It could thus provide a direct and cost-effective approach to build multi-channel photo- and biosensors, portable spectrometers, optically controlled logic circuits and computing, and high-resolution photosensing/imaging devices.

Methods

MBE growth of p-AlGaIn/n-GaN nanowires. The p-AlGaIn/n-GaN nanowires were grown on an n-type Si(111) substrate by radio-frequency plasma-assisted MBE in nitrogen-rich conditions. To remove organic contaminants, the Si substrate was thoroughly cleaned with acetone and methanol solvent. Thereafter, the native oxide on the substrate was removed by 10% hydrofluoric acid before loading into the MBE chamber. The residual oxide was then desorbed by in situ annealing of the substrate at $\sim 780^\circ\text{C}$ before growth initiation. The reflection high-energy electron diffraction with a reconstructed pattern further confirms successful clean of the Si(111) surface. Further, Al, Ga, Si and Mg fluxes were controlled using the respective thermal effusion cells, with an approximate beam equivalent pressure of 2.2×10^{-8} , 7.1×10^{-8} , 2.5×10^{-9} and 3.6×10^{-9} torr, respectively, whereas the nitrogen radicals were supplied from a radio-frequency plasma source with a forward plasma power of 350 W. The nanowires were grown with a substrate temperature at 780°C for GaN segment with Si doping and 835°C for AlGaIn segment with Mg doping.

Deposition of co-catalyst Pt nanoparticles. The co-catalyst Pt nanoparticles were deposited on the p-AlGaIn/n-GaN surface by using in situ selective photodeposition method at room temperature. Normally, the nanowire sample was immersed into a precursor solution including $100 \mu\text{l H}_2\text{PtCl}_6$ solution (20 mg ml^{-1}), 15 ml methanol and 55 ml deionized water without pH adjustment. The nanowires were then irradiated by a Hg lamp for 15 min. After Pt deposition, the sample was washed with ethanol and deionized water for more than three times and finally dried using N_2 gas. The as-obtained sample was used for material characterizations and photodetection measurement.

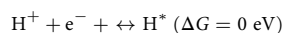
Photoelectrode preparation. Bare nanowires and Pt-decorated nanowires were further fabricated as the photoelectrode to evaluate the corresponding detection ability. To form an ohmic contact, we firstly scraped off the native oxide layer formed on the backside of the Si substrate by a diamond pen. Then, In-Ga eutectic alloy (Alfa Aesar) was deposited on the scraped area, which was subsequently mounted onto a copper sheet using a silver paste (SPI Supplies). Subsequently, the back and edge of the as-fabricated electrode device was covered by insulating epoxy to prevent current leakage, except for the nanowire surface. Finally, the photoelectrodes were cured in air at least 24 h before any measurement.

Construction of light-detection electrochemical cell. The as-prepared p-AlGaIn/n-GaN nanowire photoelectrode, Pt counter electrode and saturated Ag/AgCl reference electrode were constructed in a high-ultraviolet-transmittance quartz reaction cell (CEL-CPE50) with an electrolyte solution (here we used 0.500, 0.100, 0.050, 0.010 and 0.001 M H₂SO₄), thereby forming the light-detection electrochemical cell. Thereafter, the photodetection performance of the light-detection electrochemical cell was performed using a CHI660E electrochemical workstation with a standard three-electrode system, which was used to record the current signal and applied bias potential at room temperature. A Hg lamp was used to generate monochromatic lights with wavelengths of 254 and 365 nm to illuminate the photoelectrode. A series of LEDs with different emission wavelengths were also used for the experiments. The light intensity was calibrated by an optical power meter (Newport model 2936-R). Amperometric *I*–*t* curves were obtained at a fixed potential of 0 V with a sampling interval of 0.05 s. In this configuration, the applied voltage is set between the working and reference electrodes. Electrochemical impedance spectroscopy measurements were carried out in a frequency range from 0.1 Hz to 500,000.0 Hz with 5 mV amplitude.

Structural and spectroscopic characterization. Detailed morphologies of the as-prepared nanowires were examined using high-resolution transmission electron microscopy on JEOL-2100F systems at 200 kV and SEM on Hitachi SU8220 systems. Sub-ångström-resolution aberration-corrected HAADF-STEM measurements were acquired on a JEM-ARM200F instrument (University of Science and Technology of China) at 200 kV. EDS was performed using a 26FEI Talos F200X device at 200 kV. Room-temperature PL measurements were performed using a 266 nm excitation pulse laser. The PL signal was collected by using an ultraviolet objective and then measured by an OceanOptics QE Pro spectrometer. XPS measurements were conducted on a Thermo Scientific K-Alpha XPS instrument equipped with an Al K α source ($h\nu = 1,486.6$ eV, where h is Planck's constant and ν is the frequency) at 15 kV. The binding energy scale of all the measurements was calibrated by referencing C1s to 284.8 eV.

DFT calculation. All the related calculations based on DFT in this paper were performed by the Vienna ab initio simulation package^{40,41} with the generalized gradient approximation for the exchange–correlation potential and with the projector augmented wave. The energy cutoff for the plane-wave basis was set to 520 eV for all the calculations. The effect of the van der Waals interactions was considered by the DFT-D3 method proposed by Grimme et al.⁴². The Brillouin zones were sampled with $6 \times 6 \times 6$ and $1 \times 1 \times 1$ grids for the primitive cells of bulk phase and the surface structure according to the Monkhorst–Pack procedure, respectively. The model of the (000 $\bar{1}$) surface of AlGaIn is constructed with six Al–Ga–In layers, where the bottom three layers were fixed at the corresponding bulk structure and the dangling bonds at the bottom of the slab were passivated with hydrogen atoms. It is noteworthy that for real-world ternary nitride alloys, nitrogen atoms always occupy the anion sites, while the cations (in this work, Al and Ga) are randomly distributed among the cation sites. It was experimentally observed that different types of ordering may exist in III-nitride ternary alloys. Fortunately, the specially designed structure chosen here can well represent the microscopic structure of a random alloy for the calculation^{43,44}. Thus, an Al/Ga ratio of 3/8 was employed for the AlGaIn alloy, while the rest of the compositions were covered by quadratic regression. A vacuum layer of 15 Å was inserted between the periodically repeated slabs along the *c* axis to avoid interactions among them. A 6×6 supercell of the surface was used to investigate the adsorption of H₂. The Pt₁₀ cluster was used to decorate the surface. The structure of the Pt₁₀ cluster takes the form of a pyramid, which is the lowest-energy minimum of the gas-phase Pt₁₀ and has been used as a catalyst for the hydrogenation of styrene and CO oxidation with high catalytic activity^{45,46}. The electronic properties of bulk AlGaIn were predicted with the hybrid functional (HSE06). The geometric structures of bulk AlGaIn were relaxed until the atomic forces were less than 0.002 eV Å⁻¹ for each atom and total energies were converged to 10^{-5} eV. The optimized lattice constants are $a = 6.40$ Å and $c = 5.19$ Å, which are in agreement with the previous report⁴⁴.

Free energy calculation. In principle, an ideal HER catalyst should hold a thermal-neutral (close to 0 eV) Gibbs free energy of hydrogen adsorption ($\Delta G_{H^*} = 0$ eV). Under standard conditions, the HER pathway can be described as follows.



The Gibbs free energy of the adsorption of intermediate hydrogen (ΔG_{H^*}) on the catalyst is a key descriptor for the HER activity of the catalyst and is obtained as follows.

$$\Delta G_{H^*} = \Delta E_{H^*} + \Delta E_{ZPE} - T\Delta S_{H^*}$$

T is the temperature and ΔS_{H^*} is the entropy. Here ΔE_{ZPE} can be obtained by

$$\Delta E_{ZPE} = E_{ZPE}^{H^*} - 1/2E_{ZPE}^{H_2}$$

where $E_{ZPE}^{H^*}$ is the zero-point energy of atomic hydrogen in the catalyst and $E_{ZPE}^{H_2}$ is the zero-point energy of H₂ in the gas phase. The entropy is given by

$$S(T) = \sum_{i=1}^{3N} \left[-R \ln \left(1 - e^{-\frac{h\nu_i}{k_B T}} \right) + \frac{N_A h \nu_i}{T} \frac{e^{-h\nu_i/k_B T}}{1 - e^{-h\nu_i/k_B T}} \right],$$

where R is the universal gas constant, k_B is the Boltzmann constant, h is Planck's constant, N_A is Avogadro's number, ν_i represents the frequency and N is the number of adsorbed atoms⁴⁷.

Data availability

The data that support the plots within this paper and other findings of this study are available from the corresponding author upon reasonable request.

Received: 22 December 2020; Accepted: 29 July 2021;

Published online: 23 September 2021

References

- Zhang, Y. J. et al. Enhanced intrinsic photovoltaic effect in tungsten disulfide nanotubes. *Nature* **570**, 349–353 (2019).
- Taniyasu, Y., Kasu, M. & Makimoto, T. An aluminium nitride light-emitting diode with a wavelength of 210 nanometres. *Nature* **441**, 325–328 (2006).
- Choi, T., Lee, S., Choi, Y. J., Kiryukhin, V. & Cheong, S. W. Switchable ferroelectric diode and photovoltaic effect in BiFeO₃. *Science* **324**, 63–66 (2009).
- Bardeen, J. & Brattain, W. H. The transistor, a semi-conductor triode. *Phys. Rev.* **74**, 230 (1948).
- Xiao, K. et al. All-perovskite tandem solar cells with 24.2% certified efficiency and area over 1 cm² using surface-anchoring zwitterionic antioxidant. *Nat. Energy* **5**, 870–880 (2020).
- Lin, R. X. et al. Monolithic all-perovskite tandem solar cells with 24.8% efficiency exploiting comproportionation to suppress Sn(II) oxidation in precursor ink. *Nat. Energy* **4**, 864–873 (2019).
- Guo, F. et al. A generic concept to overcome bandgap limitations for designing highly efficient multi-junction photovoltaic cells. *Nat. Commun.* **6**, 7730 (2015).
- Essig, S. et al. Raising the one-sun conversion efficiency of III–V/Si solar cells to 32.8% for two junctions and 35.9% for three junctions. *Nat. Energy* **2**, 17144 (2017).
- Oh, N. et al. Double-heterojunction nanorod light-responsive LEDs for display applications. *Science* **355**, 616–619 (2017).
- Chen, Y. et al. Strain engineering and epitaxial stabilization of halide perovskites. *Nature* **577**, 209–215 (2020).
- Gu, L. et al. A biomimetic eye with a hemispherical perovskite nanowire array retina. *Nature* **581**, 278–282 (2020).
- García de Arquer, F. P., Armin, A., Meredith, P. & Sargent, E. H. Solution-processed semiconductors for next-generation photodetectors. *Nat. Rev. Mater.* **2**, 16100 (2017).
- Ouyang, B., Zhang, K. & Yang, Y. Photocurrent polarity controlled by light wavelength in self-powered ZnO nanowires/SnS photodetector system. *iScience* **1**, 16–23 (2018).
- Ouyang, B., Zhao, H., Wang, Z. L. & Yang, Y. Dual-polarity response in self-powered ZnO NWs/Sb₂Se₃ film heterojunction photodetector array for optical communication. *Nano Energy* **68**, 104312 (2020).
- Ouyang, B., Wang, Y. H., Zhang, R. Y., Olin, H. & Yang, Y. Dual-polarity output response-based photoelectric devices. *Cell Rep. Phys. Sci.* **2**, 100418 (2021).
- Wang, Y. J. et al. An In_{0.42}Ga_{0.58}N tunnel junction nanowire photocathode monolithically integrated on a nonplanar Si wafer. *Nano Energy* **57**, 405–413 (2019).
- Fan, S. et al. High efficiency solar-to-hydrogen conversion on a monolithically integrated InGaIn/GaN/Si adaptive tunnel junction photocathode. *Nano Lett.* **15**, 2721–2726 (2015).
- Kibria, M. G. et al. Visible light-driven efficient overall water splitting using p-type metal-nitride nanowire arrays. *Nat. Commun.* **6**, 6797 (2015).
- Seh, Z. W. et al. Combining theory and experiment in electrocatalysis: insights into materials design. *Science* **355**, 6321 (2017).
- Chen, S. S., Takata, T. & Domen, K. Particulate photocatalysts for overall water splitting. *Nat. Rev. Mater.* **2**, 17050 (2017).
- He, Y. M. et al. Dependence of interface energetics and kinetics on catalyst loading in a photoelectrochemical system. *Nano Res.* **12**, 2378–2384 (2019).
- Zhou, B. et al. Gallium nitride nanowire as a linker of molybdenum sulfides and silicon for photoelectrocatalytic water splitting. *Nat. Commun.* **9**, 3856 (2018).
- Wenderich, K. & Mul, G. Methods, mechanism, and applications of photodeposition in photocatalysis: a review. *Chem. Rev.* **116**, 14587–14619 (2016).
- Li, Z. et al. Surface-polarity-induced spatial charge separation boosts photocatalytic overall water splitting on GaN nanorod arrays. *Angew. Chem. Int. Ed.* **132**, 945–952 (2020).

25. Takata, T. et al. Photocatalytic water splitting with a quantum efficiency of almost unity. *Nature* **581**, 411–414 (2020).
26. Li, R. et al. Spatial separation of photogenerated electrons and holes among {010} and {110} crystal facets of BiVO₄. *Nat. Commun.* **4**, 1432 (2013).
27. Kibria, M. G. et al. Tuning the surface Fermi level on p-type gallium nitride nanowires for efficient overall water splitting. *Nat. Commun.* **5**, 3825 (2014).
28. Cao, L. et al. Atomically dispersed iron hydroxide anchored on Pt for preferential oxidation of CO in H₂. *Nature* **565**, 631–635 (2019).
29. Wang, Y. J. et al. A single-junction cathodic approach for stable unassisted solar water splitting. *Joule* **3**, 2444–2456 (2019).
30. Varadhan, P. et al. Surface passivation of GaN nanowires for enhanced photoelectrochemical water-splitting. *Nano Lett.* **17**, 1520–1528 (2017).
31. Chowdhury, F. A., Trudeau, M. L., Guo, H. & Mi, Z. A photochemical diode artificial photosynthesis system for unassisted high efficiency overall pure water splitting. *Nat. Commun.* **9**, 1707 (2018).
32. Cao, Y. et al. Atomic-level insight into optimizing the hydrogen evolution pathway over a Co₁-N₄ single-site photocatalyst. *Angew. Chem. Int. Ed.* **56**, 12191–12196 (2017).
33. Liu, W. et al. Single-site active cobalt-based photocatalyst with a long carrier lifetime for spontaneous overall water splitting. *Angew. Chem. Int. Ed.* **129**, 9440–9445 (2017).
34. Klahr, B., Gimenez, S., Fabregat-Santiago, F., Bisquert, J. & Hamann, T. W. Photoelectrochemical and impedance spectroscopic investigation of water oxidation with 'Co–Pi'-coated hematite electrodes. *J. Am. Chem. Soc.* **134**, 16693–16700 (2012).
35. Dotan, H., Sivula, K., Grätzel, M., Rothschild, A. & Warren, S. C. Probing the photoelectrochemical properties of hematite (α-Fe₂O₃) electrodes using hydrogen peroxide as a hole scavenger. *Energy Environ. Sci.* **4**, 958–964 (2011).
36. Ma, N., Zhang, K. & Yang, Y. Photovoltaic–pyroelectric coupled effect induced electricity for self-powered photodetector system. *Adv. Mater.* **29**, 1703694 (2017).
37. Jiang, H. P., Su, Y. J., Zhu, J., Lu, H. M. & Meng, X. K. Piezoelectric and pyroelectric properties of intrinsic GaN nanowires and nanotubes: size and shape effects. *Nano Energy* **45**, 359–367 (2018).
38. Ra, Y. H. et al. An electrically pumped surface-emitting semiconductor green laser. *Sci. Adv.* **6**, eaav7523 (2020).
39. Xie, Z. J. et al. Ultrathin 2D nonlayered tellurium nanosheets: facile liquid-phase exfoliation, characterization, and photoresponse with high performance and enhanced stability. *Adv. Funct. Mater.* **28**, 1705833 (2018).
40. Kresse, G. & Furthmüller, J. Efficiency of ab-initio total energy calculations for metals and semiconductors using a plane-wave basis set. *Comput. Mater. Sci.* **6**, 15–50 (1996).
41. Kresse, G. & Furthmüller, J. Efficient iterative schemes for ab initio total-energy calculations using a plane-wave basis set. *Phys. Rev. B* **54**, 11169–11186 (1996).
42. Grimme, S. Semiempirical GGA-type density functional constructed with a long-range dispersion correction. *J. Comput. Chem.* **27**, 1787–1799 (2006).
43. Bernardini, F. & Fiorentini, V. Nonlinear macroscopic polarization in III-V nitride alloys. *Phys. Rev. B* **64**, 085207 (2001).
44. Liu, K. K. et al. Wurtzite BAlN and B GaN alloys for heterointerface polarization engineering. *Appl. Phys. Lett.* **111**, 222106 (2017).
45. Yin, C. R. et al. Alumina-supported sub-nanometer Pt₁₀ clusters: amorphization and role of the support material in a highly active CO oxidation catalyst. *J. Mater. Chem. A* **5**, 4923–4931 (2017).
46. Imaoka, T. et al. Platinum clusters with precise numbers of atoms for preparative-scale catalysis. *Nat. Commun.* **8**, 688 (2017).
47. Zhu, Y. A., Chen, D., Zhou, X. G. & Yuan, W. K. DFT studies of dry reforming of methane on Ni catalyst. *Catal. Today* **148**, 260–267 (2009).

Acknowledgements

This work was funded by the National Natural Science Foundation of China (grant nos. 61905236 and 51961145110), the Fundamental Research Funds for the Central Universities (grant no. WK2100230020), USTC Research Funds of the Double First-Class Initiative (grant no. YD3480002002) and USTC National Synchrotron Radiation Laboratory (grant no. KY2100000099), and was partially carried out at the USTC Center for Micro and Nanoscale Research and Fabrication. We thank W. Wu from USTC for the support of DFT calculation.

Author contributions

H.S. developed the idea and designed the experiments. D.W., X.L., Y.K., Y.W., S.F., H.Y., M.H.M., H.Z. and Z.M. performed the MBE growth and characterizations, XPS measurement and photodetection experiments, as well as collected and analysed the data. D.W., X.L., Y.K. and S.F. performed Pt nanoparticle decoration and material investigation. X.W. and W.H. conducted and discussed the theoretical calculations. D.W. and H.S. performed the aberration-corrected STEM characterization. D.W., L.F., S.L. and H.S. co-wrote the paper. All the authors discussed the results and commented on the manuscript.

Competing interests

The authors declare no competing interests.

Additional information

Supplementary information The online version contains supplementary material available at <https://doi.org/10.1038/s41928-021-00640-7>.

Correspondence and requests for materials should be addressed to Haiding Sun.

Peer review information *Nature Electronics* thanks Ya Yang and Daoyou Guo for their contribution to the peer review of this work.

Reprints and permissions information is available at www.nature.com/reprints.

Publisher's note Springer Nature remains neutral with regard to jurisdictional claims in published maps and institutional affiliations.

© The Author(s), under exclusive licence to Springer Nature Limited 2021